CHAPTER V

RESULTS AND DISCUSSIONS

PART (A)

V-A-1- DC Electrical conductivity measurements:

DC electrical conductivity measurements as a function of temperature were measured for all the samples at a temperature rang of 10-300 K. Table (V-A-1) shows different measured T_c of the prepared samples. $T_{c,H}$ is a critical temperature for the high T_c phase, $T_{c,L}$ is a critical temperature for the low T_c phase and $T_{c,off}$ is a zero resistance transition temperature. The zero resistance $T_{c,off}$ was defined as the temperature at which the resistance is approximately vanished in the sample, i.e. zero resistance.

(a) sample EM1:

Figure (V-A-1) shows the temperature dependence of the electrical resistance for the sample EM1 (Bi-Sr-Ca-Cu) which has a composition (1:1:1:2). The resistance initially decreases linearly with decreasing the temperature, which is characteristic for the sample having metallic behavior. This liner behavior is observed from 300 K down to 120 K, which is in agreement with that reported by Mori et al.[25] for the same composition annealed in 10 hours. On Further cooling, a sharp drop occurs at about 100 K, reaching a zero resistance

Table (V-A-1): The critical temperatures ($T_{c,H}$, $T_{c,L}$, $T_{c,off}$) for the Prepared samples.

Symbol of the samples	Composition	$T_{c,H}$ (K)	$T_{c,L}$ (K)	$T_{c,off}$ (K)
EM1	Bi:Sr:Ca:Cu 1:1:1:2	120	80	58
EM2	Bi:Pb:Sr:Ca:Cu 2:0.3:2:2:3	125	80	73
EM3	Bi:Pb:Sr:Ca:Cu 2:0.3:2:2:3	120	75	52
EM4	Bi:Pb:Sr:Ca:Cu 2:0.5:2:2:3	125	85	54
EM5	Bi:Ba:Sr:Ca:Cu 2:0.3:2:2:3	120	72	64
EM6	Bi:Pb:Sr:Ca:Cu 2:0.3:2.2:2:3.2	135	85	58

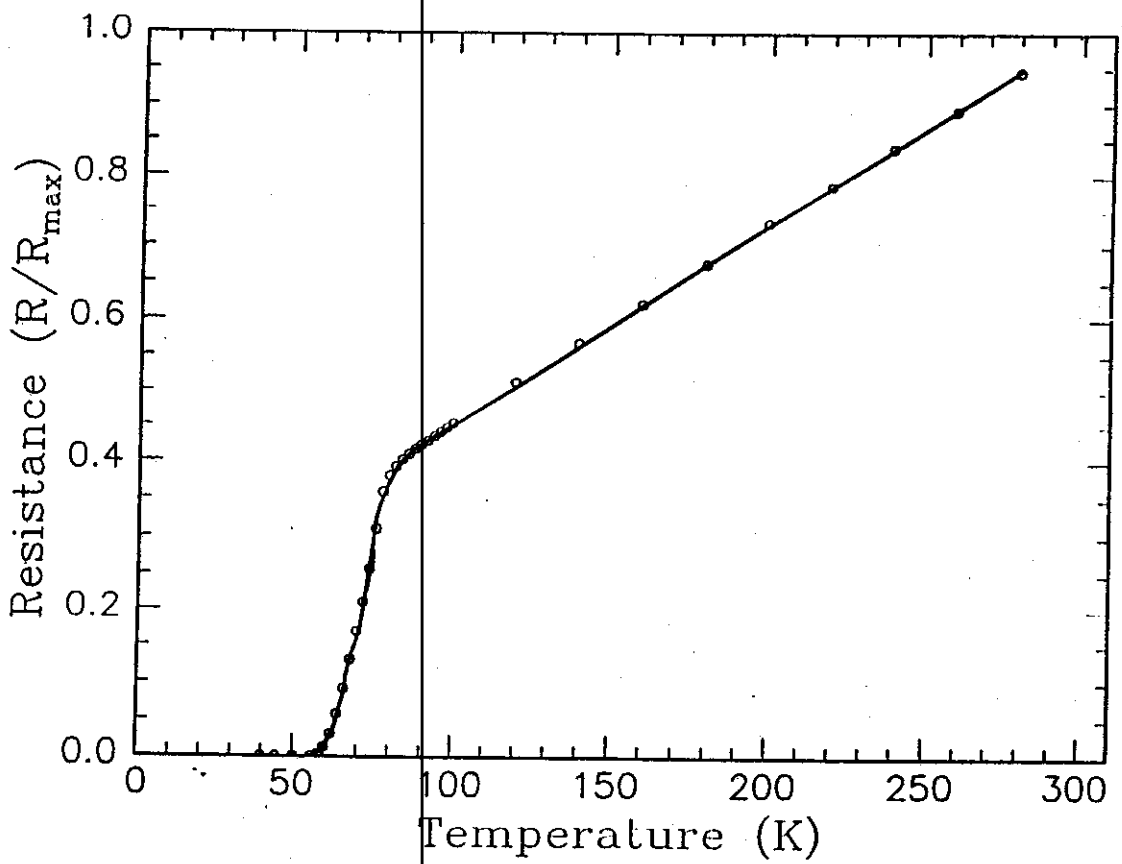

Figure (V-A-1): Temperature dependence of the electrical resistance for sample EM1.

level at a temperature 58 K. This temperature is lower than that reported by Mori et al.[25] by about 30 K. It means that increasing annealing time will lead to shift the T_c to lower value.

(b) sample EM2:

Figure (V-A-2) shows the results of electrical resistance measurements for sample EM2 (Bi-Pb-Sr-Ca-Cu) which has a composition (2:0.3:2:2:3). The resistance curve has been shown two-step transitions. The resistance decreases linearly with decreasing the temperature from 300 K till 120 K (metallic behavior) and below this temperature it starts to deviate from linearity, indicating the presence of two superconducting phases (2212) and (2223) as reported in X-ray results. The temperature range observed here is less than that reported by Jao et al,[37] This shift may be related to the different in annealing process. The first superconducting transition begins at 125 K and the second superconducting transition begins at 80 K for the sample EM2, annealed at 1143 K for 10 days. Zero resistance observed at 73 K.

(c) Sample EM3:

The electrical resistance of the sample EM3 (Bi-Pb-Sr-Ca-Cu) which has a composition (2:0.3:2:2:3) is shown in Figure (V-A-3).

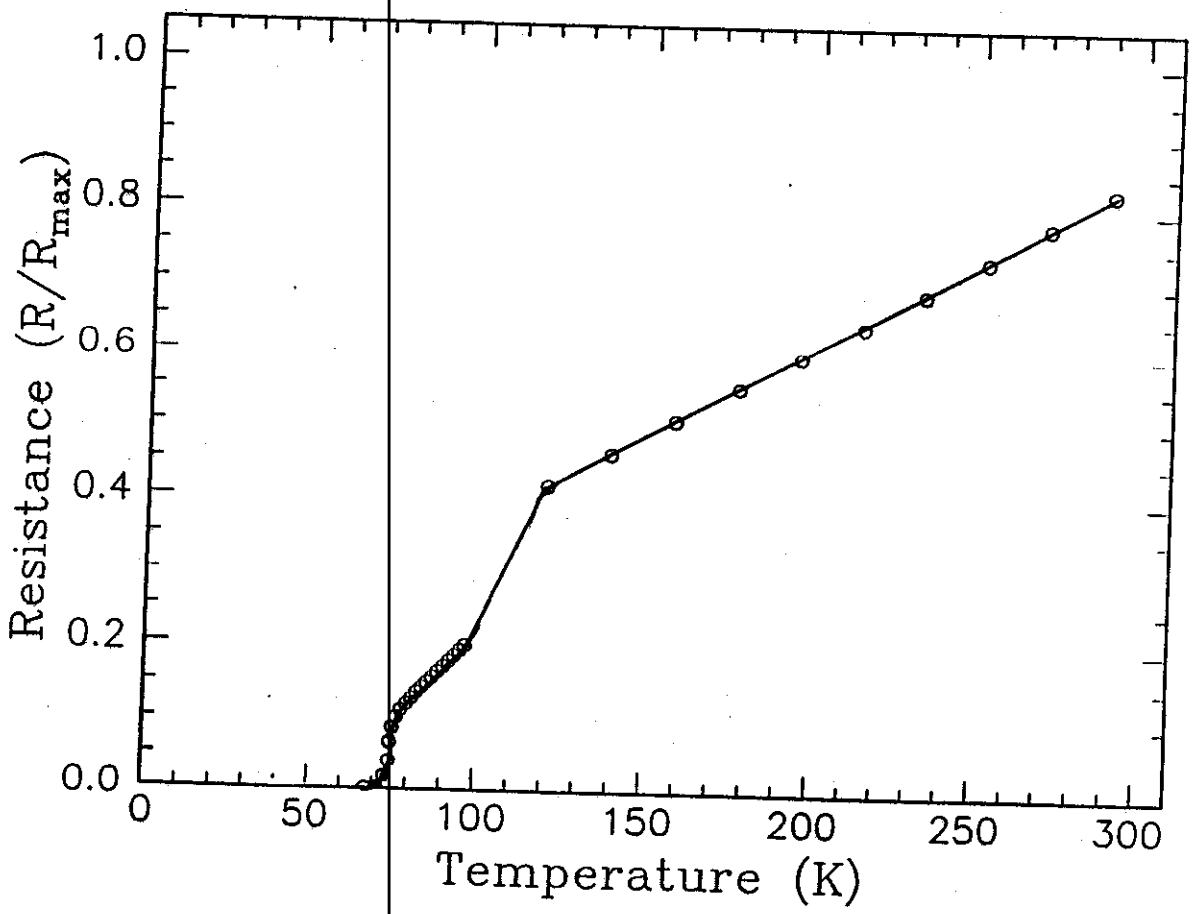

Figure (V-A-2): Temperature dependence of the electrical resistance for sample EM2.

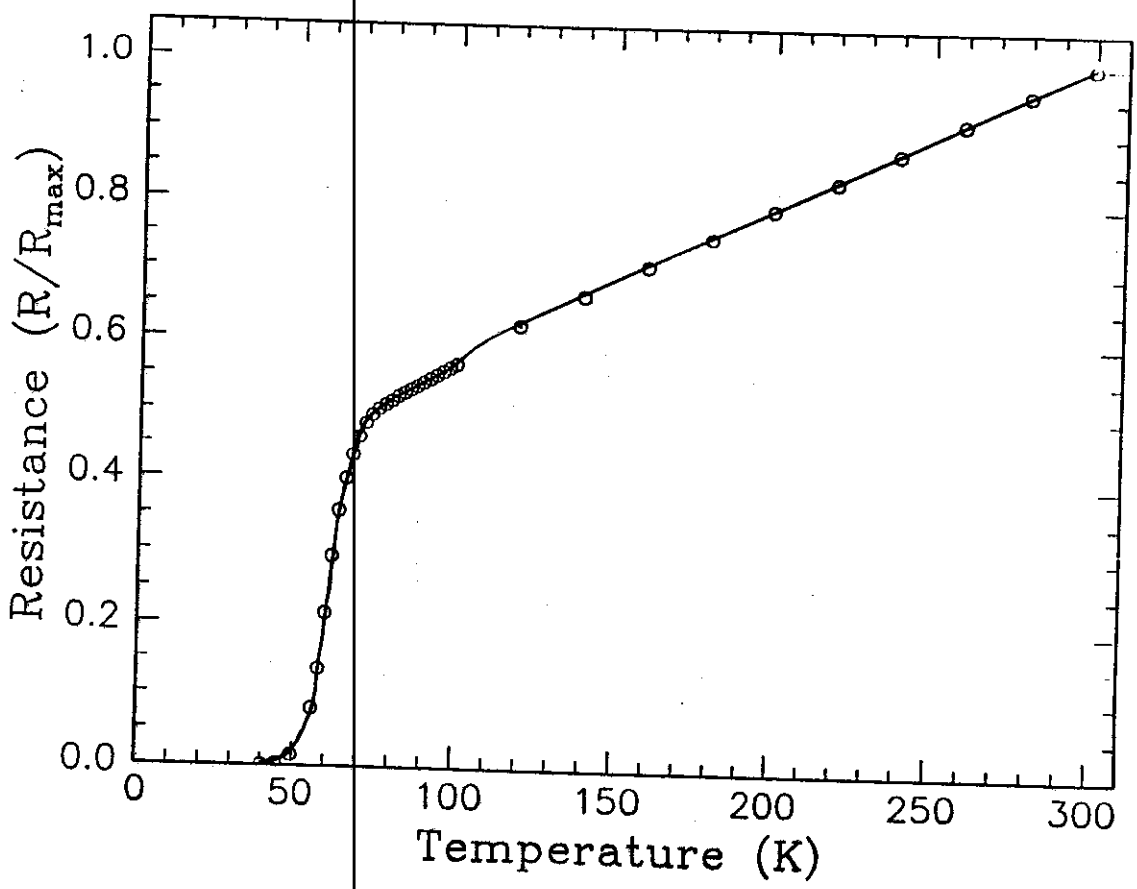

Figure (V-A-3): Temperature dependence of the electrical resistance for sample EM3.

The resistance decreases linearly with decreasing temperature (metallic behavior). The sample exhibits a small drop in resistance for the high superconducting phase with $T_{c,H}$ at around 120 K, however, the lower superconducting phase transition $T_{c,L}$ appearing at around 75 K. Sample showed zero resistance state $T_{c,off}$ at 52 K. This sample has the same composition of EM2 but annealed at shorter time, see Table (V-A-2). The decrease in the $T_{c,off}$ of the sample EM3 is attributed here to the decreasing in the annealing time. This is in contrary with that reported above for sample EM1.

(d) Sample EM4:

Figure (V-A-4) shows the temperature dependence of the electrical resistance for the sample EM4, which has a higher concentration of lead than that presents in samples EM2 and EM3, (Bi-Pb-Sr-Ca-Cu) with a composition of (2:0.5:2:2:3). As the temperature is lowered, the resistance initially decreases linearly, which is characteristic of a metal having ohmic behavior. The superconducting transitions $T_{c,H}$ and $T_{c,L}$ begin at 125 K and 85 K respectively. The sample shows zero resistance ($T_{c,off}$) at 54 K.

(e) Sample EM5:

The electrical resistance of the sample EM5 (Bi-Ba-Sr-Ca-Cu), which

Table (V-A-2): Composition, annealing time and different T_c's of the prepared samples.

Symbol of the samples	Composition	Annealing time/day	$T_{c,off}$ (K)
EM1	Bi:Sr:Ca:Cu 1: 1 : 1 : 2	10	58
EM2	Bi:Pb:Sr:Ca:Cu 2 : 0.3 : 2 : 2: 3	10	73
EM3	Bi:Pb:Sr:Ca:Cu 2 : 0.3 : 2 : 2 : 3	3	52
EM4	Bi:Pb:Sr:Ca:Cu 2 : 0.5: 2 : 2: 3	10	54
EM5	Bi:Ba:Sr:Ca:Cu 2 : 0.3: 2 : 2: 3	3	64
EM6	Bi:Pb:Sr:Ca:Cu 2: 0.3: 2.2 : 2 :3.2	3	58

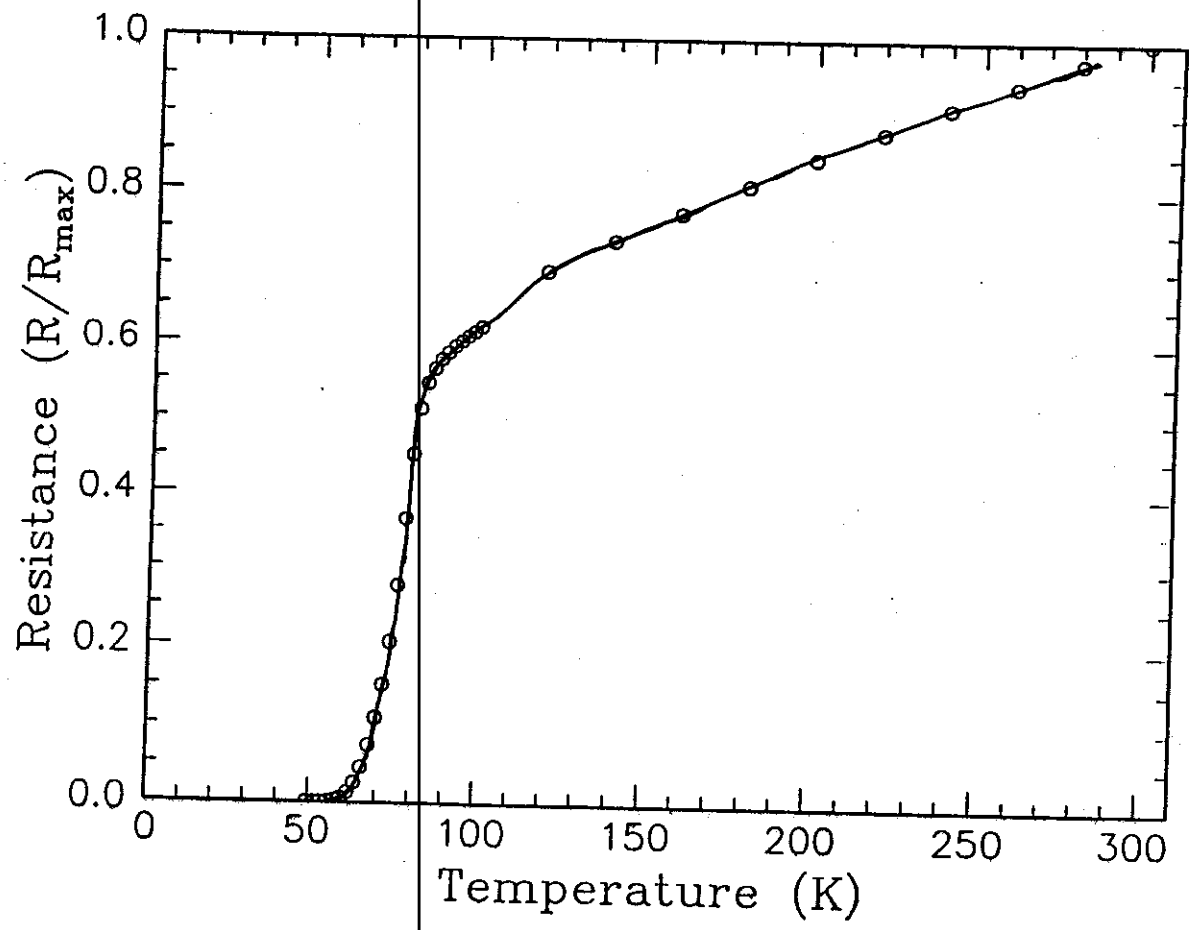

Figure (V-A-4): Temperature dependence of the electrical resistance for sample EM4.

has different composition than other samples, has been investigated. It contains Ba^{2+} which has not been studied by others. The sample has a composition of (2:0.3:2:2:3). Figure (V-A-5) shows that the resistance varies linearly from 300 K till 125 K and below this temperature it starts to deviate from linearity indicating the presence of two superconducting phases (2212) and (2223). The superconducting transition begins at 80 K for the sample EM5. Zero resistance observed at 63 K. The value of T_c here was improved higher than that obtained in sample EM3.

(f) Sample EM6:

Figure (V-A-6) shows the temperature dependence of the electrical resistance for the sample EM6 (Bi-Pb-Sr-Ca-Cu) which has a composition (2:0.3:2:2.2:3.2). The resistance decreases linearly with decreasing temperature. The sample exhibits a small drop in resistance at around 120 K; however, the sample showed zero resistance state at 58 K. Joa et al. [37] reported the same result.

In order to investigate the effect of the concentration of the superconducting phases which is formed in the samples, the T_c-values have been plotted against the relative concentration of each superconducting phase, Figures (V-A-7), (V-A-8). No relation could

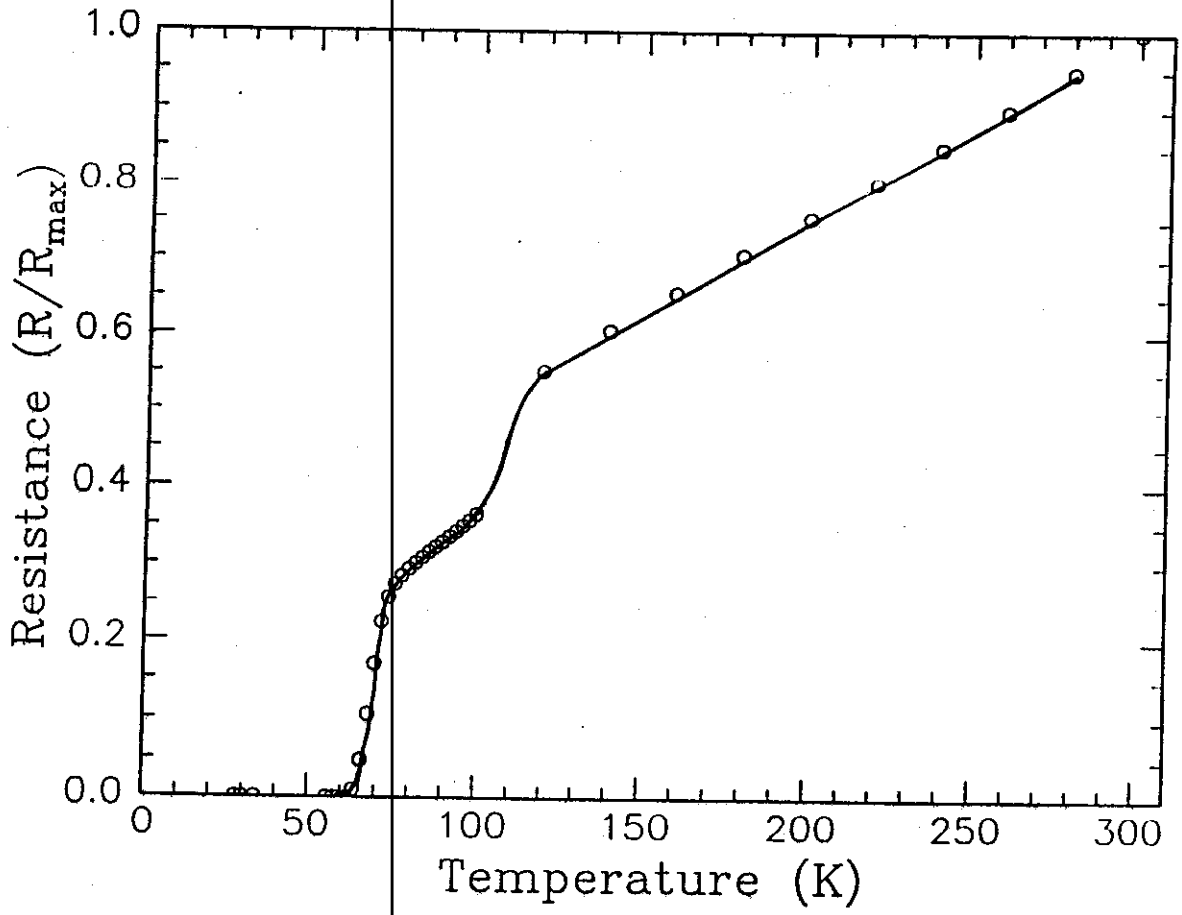

Figure (V-A-5): Temperature dependence of the electrical resistance for sample EM5.

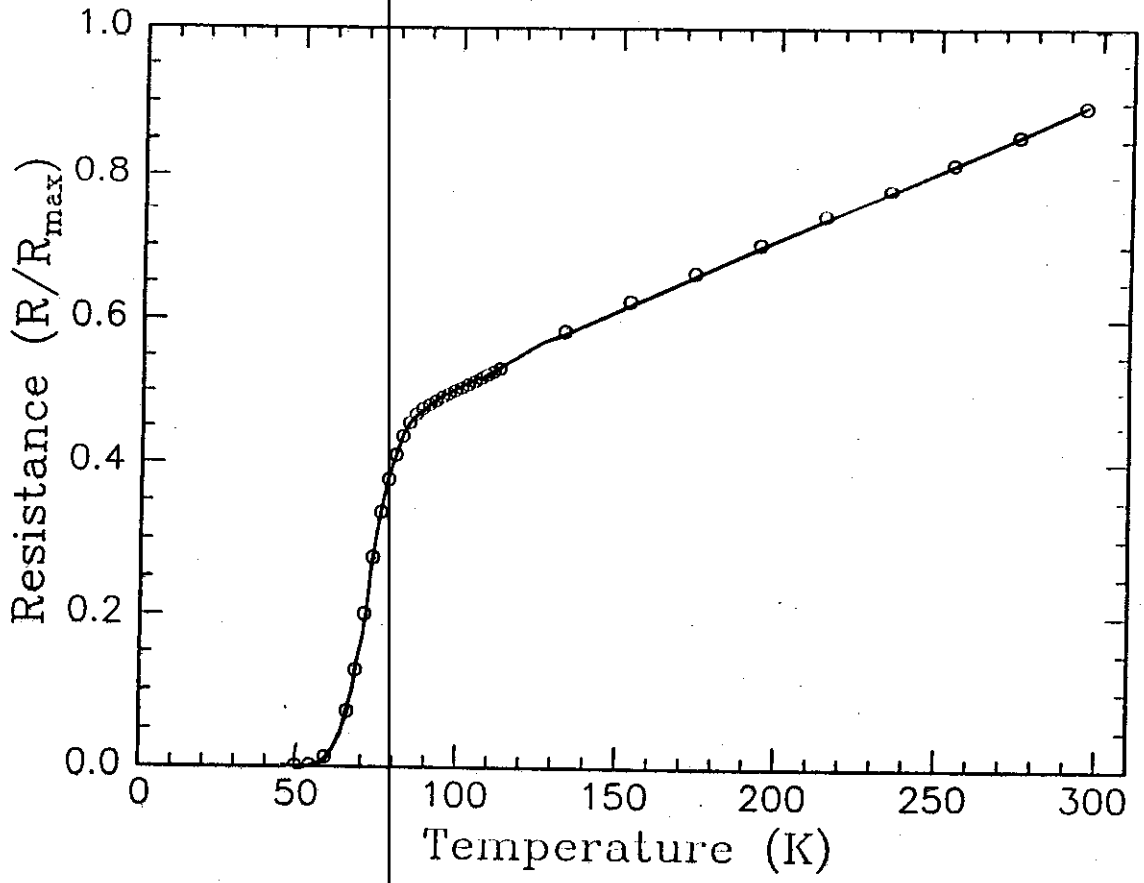

Figure (V-A-6): Temperature dependence of the electrical resistance for sample EM6.

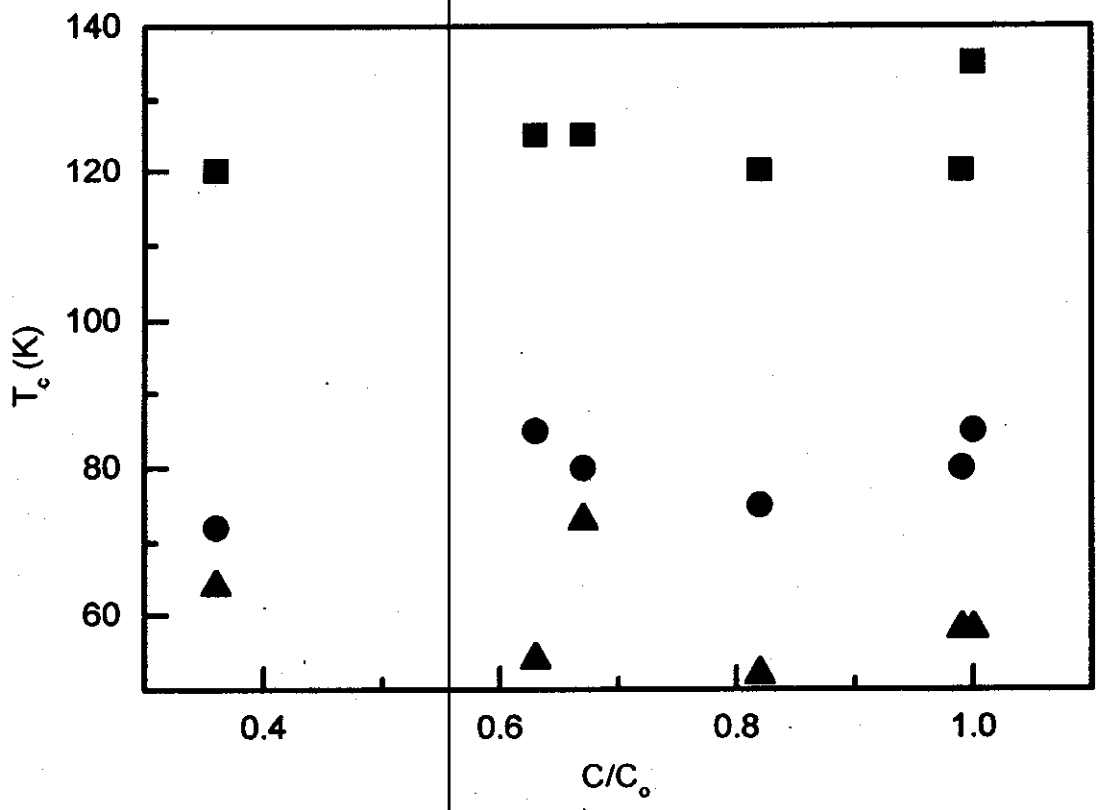

Figure (V-A-7): The T_c-values verses the relative concentration of the superconducting phase (2212) for all the prepared samples. ■ $T_{c,H}$, ● $T_{c,L}$, ▲ $T_{c,off}$.

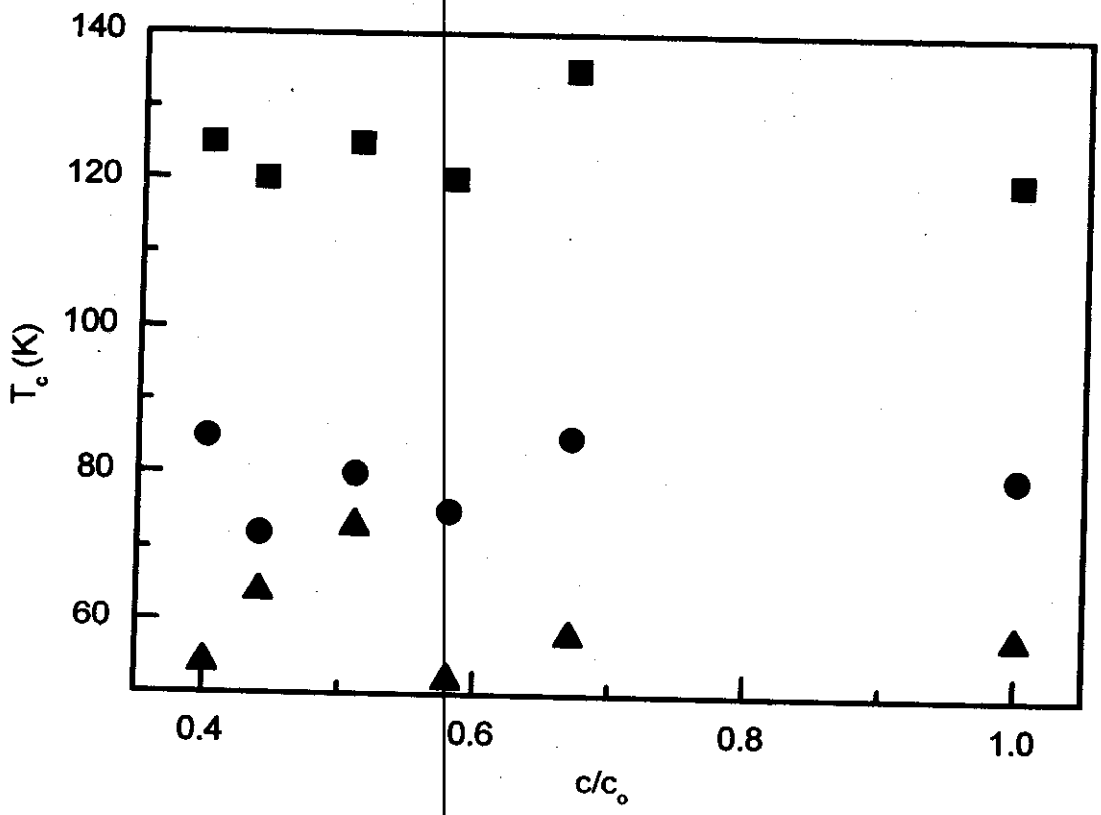

Figure (V-A-8): The T_c-values verses the relative concentration of the superconducting phase (2223) for all the prepared samples. ■ $T_{c,H}$, ● $T_{c,L}$, ▲ $T_{c,off}$.

be observed between T_c-values and C/C_o for the two phases 2212, 22223. This refers to that the superconducting phases are not only the factor which affecting the shift in T_c-values as reported by Tarascon et al[11].

V-A-2- DC Magnetic measurements:

The magnetic susceptibility was carried out in the SQUID magnetometer. Each scan consists of two branches marked by ZFC (zero-field-cooled) and FC (field-cooled). ZFC corresponds to initially cooling the sample in zero field and then the field was applied; the magnetization M versus temperature T is then measured while warming the samples up from 10 K up to 120 K. However, FC corresponds to cooling the sample in the presence of the field. The magnetic measurements were carried out for all the samples at a magnetic field strength of 5 Gauss. The main results of magnetic measurements are summarized and given in Table (V-A-3).

(a) Sample EM1:

Figure (V-A-9) shows temperature dependence of magnetization for sample EM1. These data give strong evidence for bulk superconductivity at high temperatures. The signal shows a negative

Table (V-A-3): Magnetic results of the investigated samples.

Sample symbol	Composition	Annealing time/day	T_{irr}	Difference between (ZFC) and (FC). (EMU× 10^{-3})
EM1	Bi:Sr:Ca:Cu 1: 1 : 1 : 2	10	78	- 9.29
EM2	Bi:Pb:Sr:Ca:Cu 2 : 0.3 : 2 : 2: 3	10	80	- 8.32
EM3	Bi:Pb:Sr:Ca:Cu 2 : 0.3 : 2 : 2 : 3	3	71	- 7.97
EM4	Bi:Pb:Sr:Ca:Cu 2 : 0.5: 2 : 2: 3	10	79	- 7.87
EM5	Bi:Ba:Sr:Ca:Cu 2 : 0.3: 2 : 2: 3	3	108	- 3.29
EM6	Bi:Pb:Sr:Ca:Cu 2: 0.3: 2.2 : 2 :3.2	3	79	- 8.81

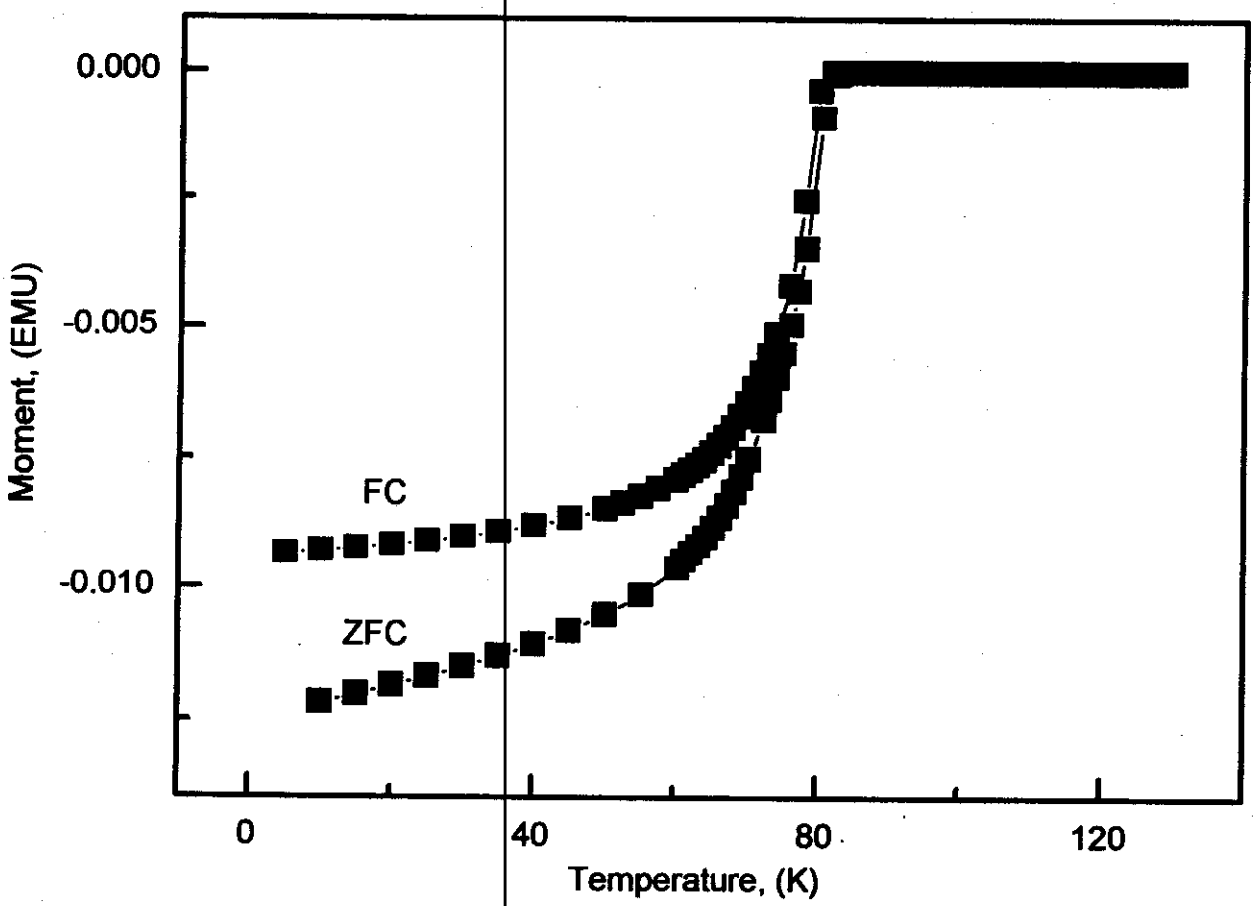

Figure (V-A-9): The field-cooled (FC) and the zero field-cooled (ZFC) magnetic moment for sample EM1 in a 5 G field.

values which indicates the diamagnetic character. The transition in the ZFC and FC for sample EM1 is sharp, showing a midpoint at 81 K.

It should be noted that at this field the irreversibility temperature T_{irr} (temperature at which the values of ZFC and FC coincide) occurs at $T_{irr} = 78$ K. The difference between ZFC and FC values is about -9.29×10^{-3} EMU. The sample is considered to be in superconducting state at $T < 58$ K. The observed superconductivity is probably bulk in nature, although the superconducting state is not formed over the whole specimen (comparing with that observed for perfect diamagnetic material with $\chi = -1/4\pi$)[123]. The broad transition observed is probably due to inhomogenaity of the sample, as frequently observed in other oxide superconductors. Thus, the results of the magnetic susceptibility indicate to the presence of many phases and referring to that at high T_c superconducting state is certainly realized in a part of the sample.

(b) Sample EM2:

Figure (V-A-10) shows temperature dependence of magnetization for sample EM2. Diamagnetism due to the Meissner effect is clearly seen at and below 78 K. The transition in the ZFC and FC for sample EM2 showing at 78 K. The difference between ZFC and FC values is about -8.32×10^{-3} EMU

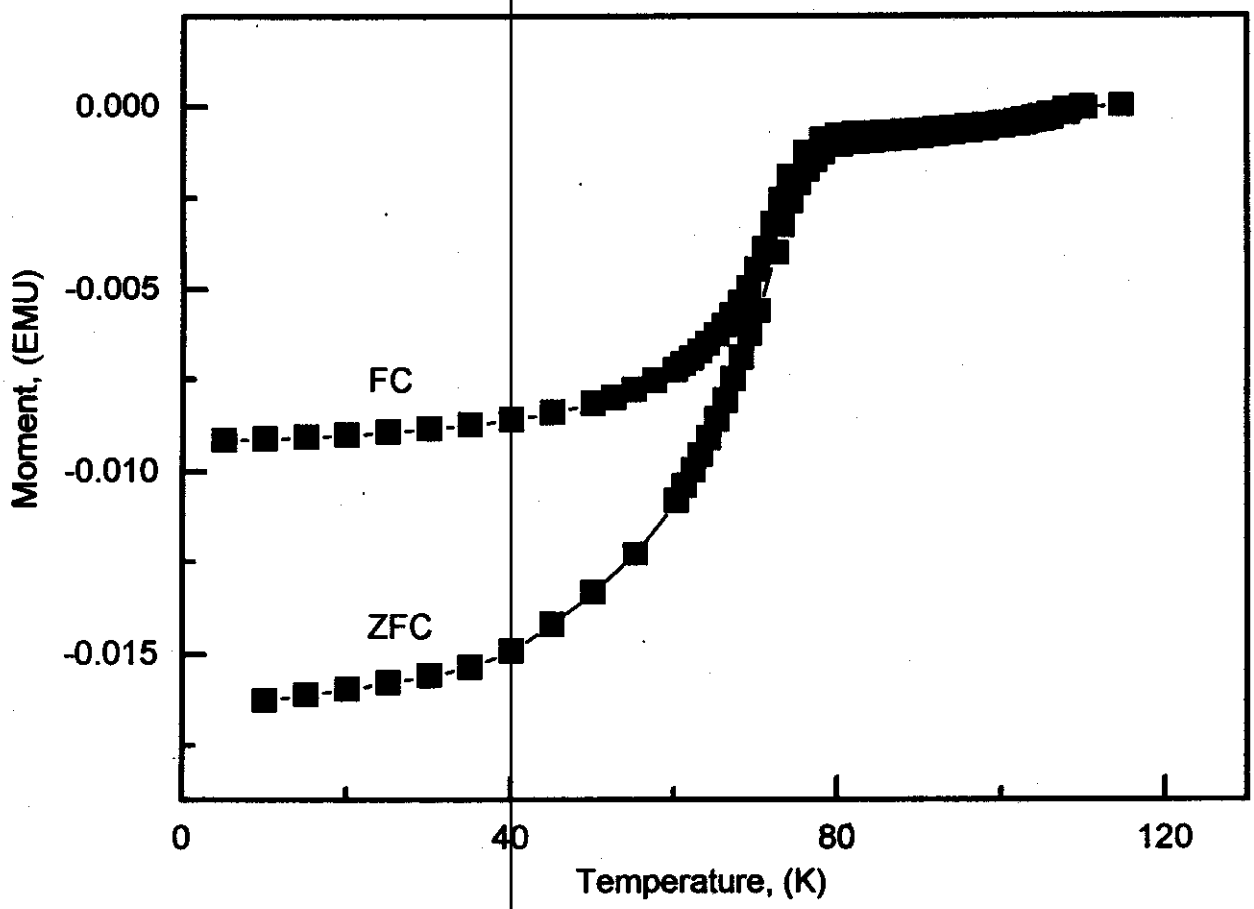

Figure (V-A-10): The field-cooled (FC) and the zero field-cooled (ZFC) magnetic moment for sample EM2 in a 5 G field.

(c) Sample EM3:

Figure (V-A-11) shows temperature dependence of magnetization for sample EM3. The sample has a diamagnetic properties. The transition in the ZFC and FC for the sample occurred at 72 K. The difference between ZFC and FC values is about -7.97×10^{-3} EMU.

(d) Sample EM4:

Figure (V-A-12) shows temperature dependence of magnetization for sample EM4. Diamagnetism due to the Meissner effect is clearly seen at and below 81 K. The difference between ZFC and FC values is about -7.87×10^{-3} EMU.

(e) Sample EM5:

Figure (V-A-13) shows temperature dependence of magnetization for sample EM5. The sample exhibits diamagnetic response due to the Meissner effects. ZFC and FC dc-magnetization curves show two transitions, first transition at 107 K and the second at 73 K. The difference between ZFC and FC values is about -3.29×10^{-3} EMU.

(f) Sample EM6:

Figure (V-A-14) shows temperature dependence of magnetization for sample EM6. The signal shows that the sample has diamagnetic

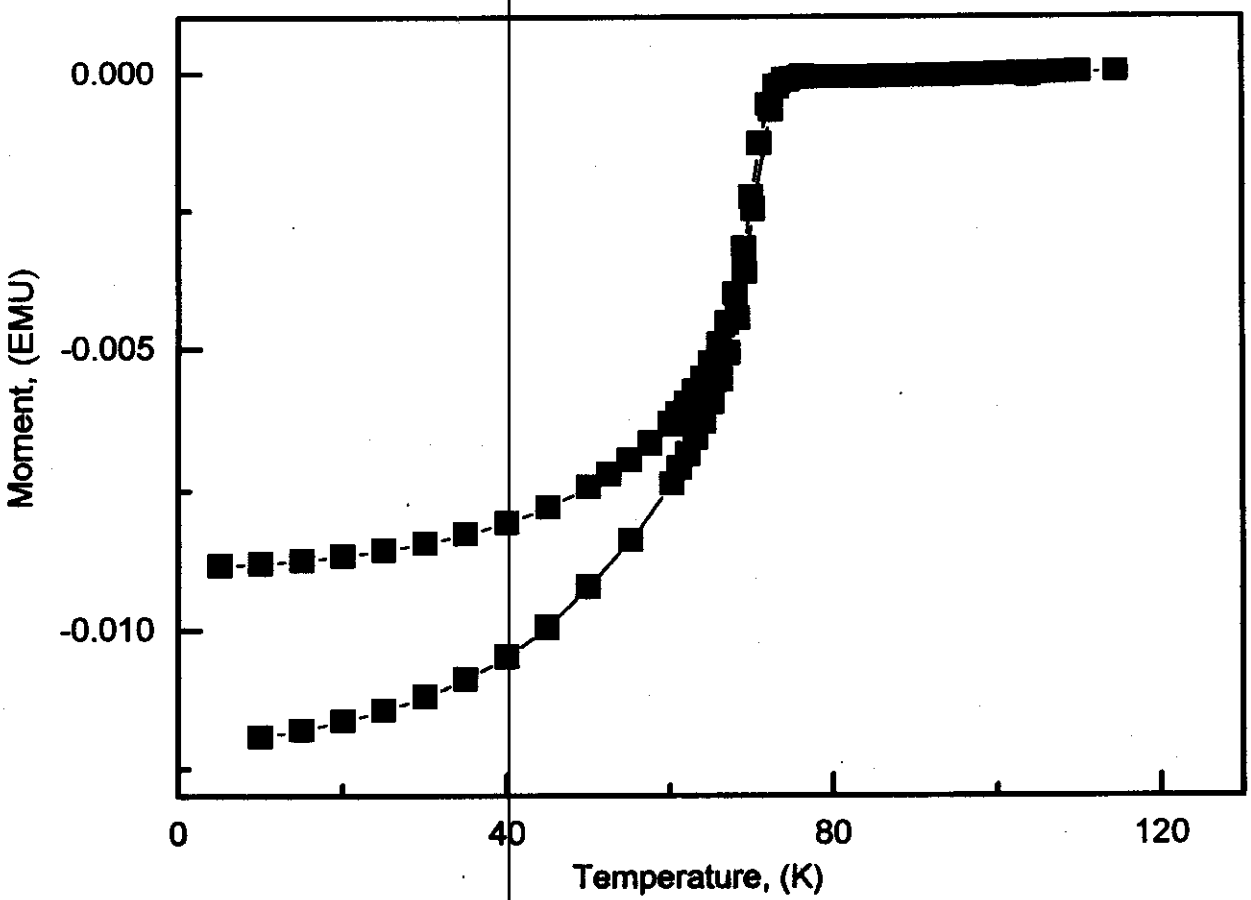

Figure (V-A-11): The field-cooled (FC) and the zero field-cooled (ZFC) magnetic moment for sample EM3 in a 5 G field.

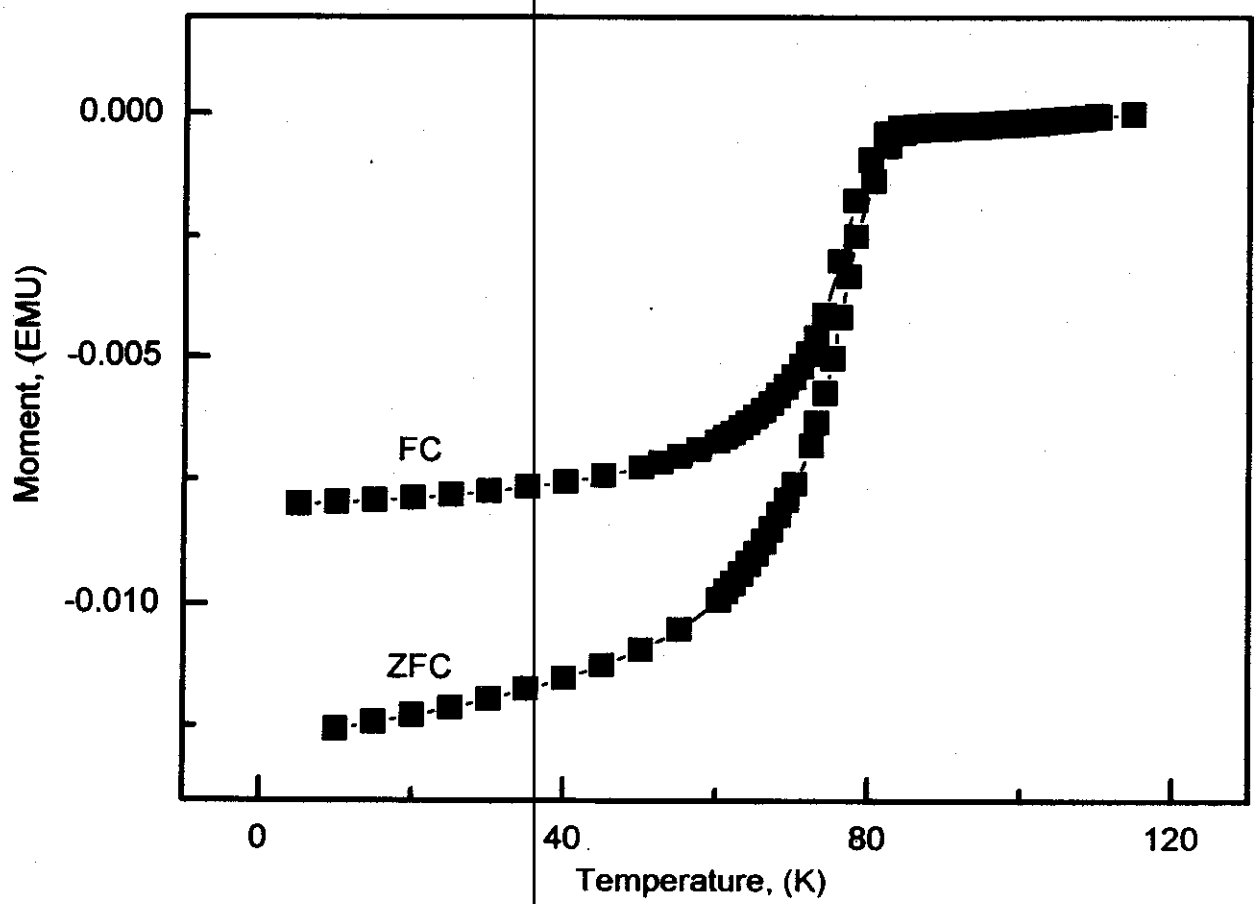

Figure (V-A-12): The field-cooled (FC) and the zero field-cooled (ZFC) magnetic moment for sample EM4 in a 5 G field.

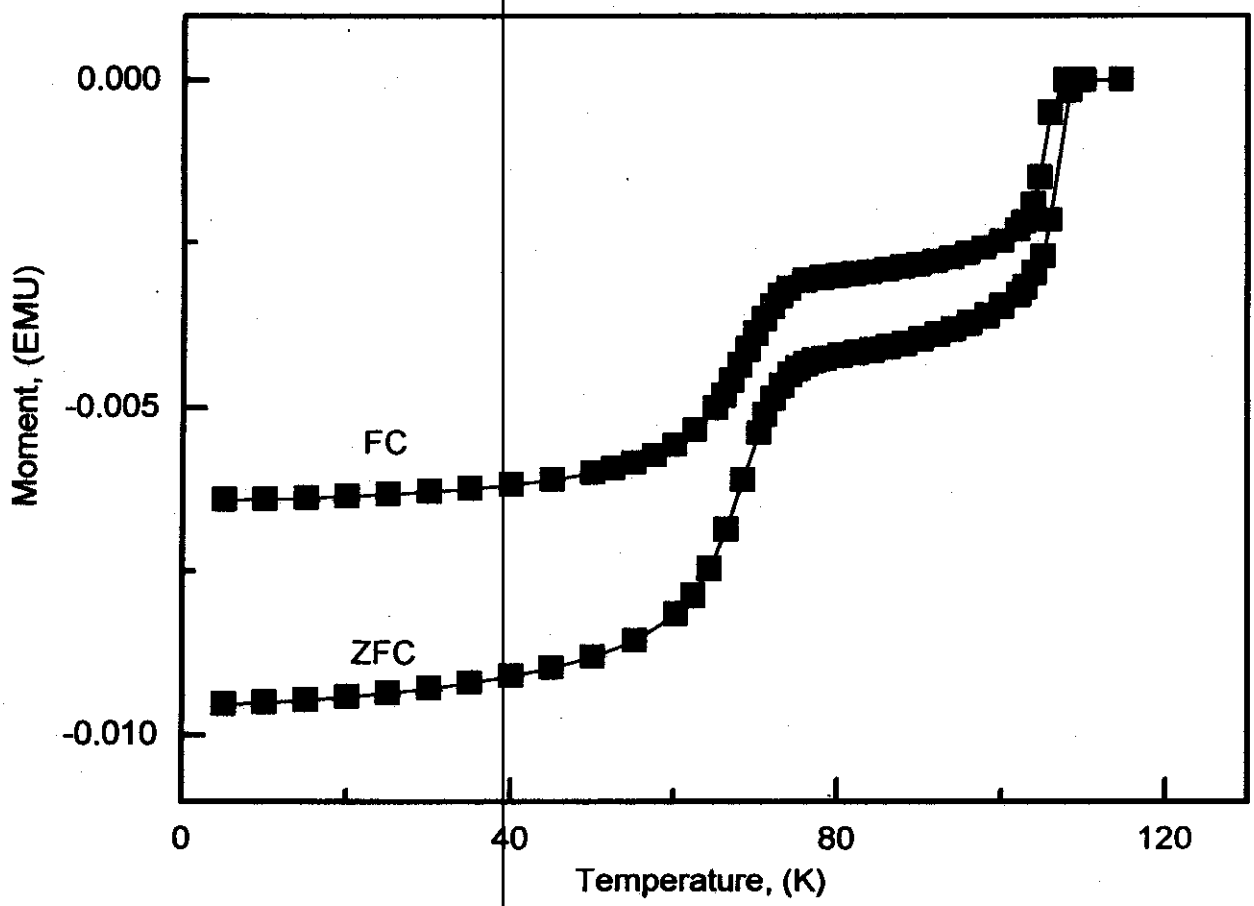

Figure (V-A-13): The field-cooled (FC) and the zero field-cooled (ZFC) magnetic moment for sample EM5 in a 5 G field.

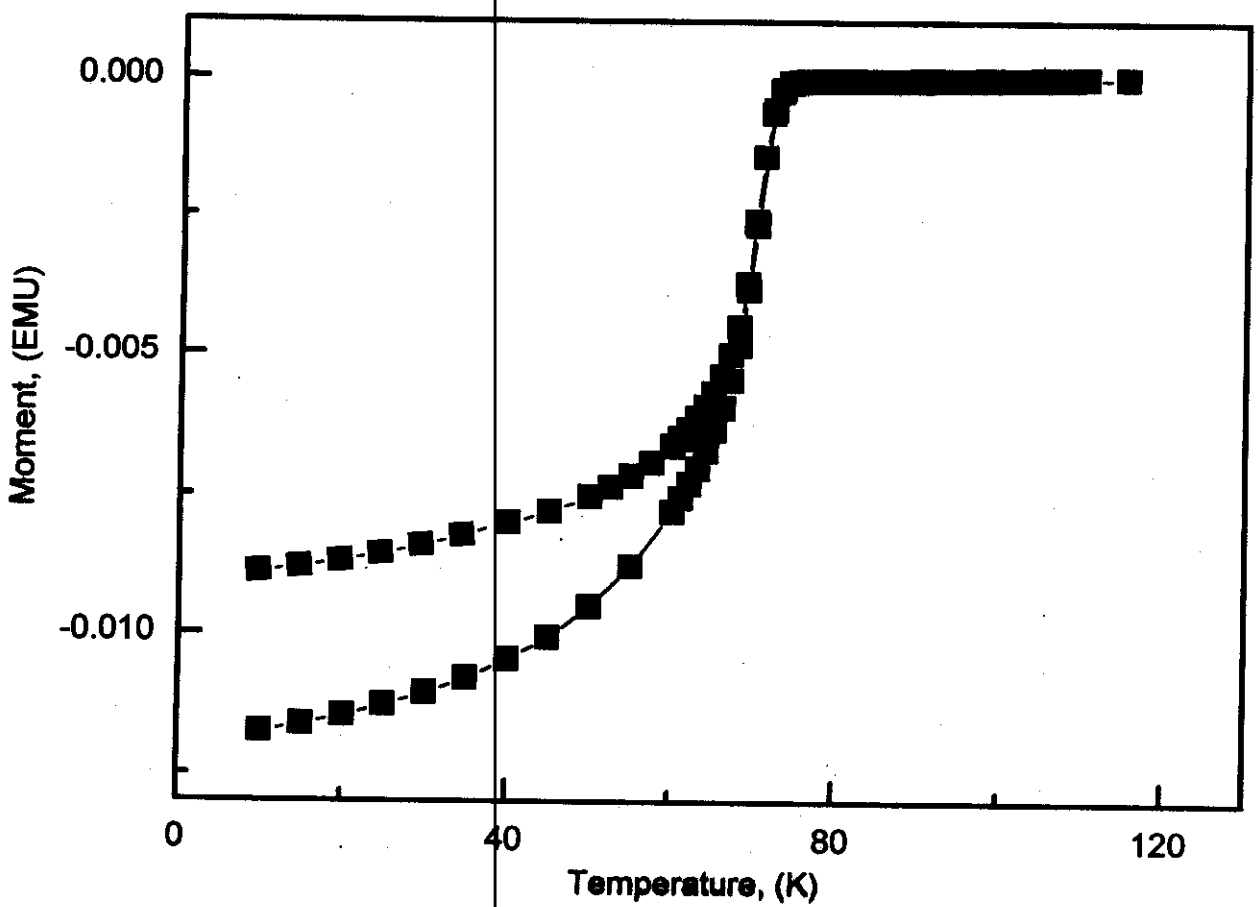

Figure (V-A-14): The field-cooled (FC) and the zero field-cooled (ZFC) magnetic moment for sample EM6 in a 5 G field.

properties. The ZFC and the FC dc-magnetization curves show a transition at 73 K. The difference between ZFC and FC values is about -8.81×10^{-3} EMU.

Table (V-A-3) shows that the difference between flux exclusion (ZFC – values) and flux expulsion (FC – values) and the T_{irr} –values are larger for sample EM5 which contains Ba^{+2} and has nearly the same values for other samples. These results refer to the presence of large trapping and pinning of different superconducting phase at the low magnetic field due to the presence of Ba^{+2}. This goes in parallel way with the large size and small grains observed for the morphology of the sample EM5 containing Ba^{+2} ion (Figure IV-11).

V-A-3 General Discussion:

In the present work, different BSCCO samples have been used in order to compare their superconducting properties in each case. The dc electrical conductivity measurements showed that, all the prepared samples are superconductors with different T_c depending on the composition and the annealing time for the samples. Also the bulk superconductivity for our samples were confirmed by observation of both diamagnetic shielding and Meissner signal. Based on the experimental results described above, the obtained T_c's appear to be quite sensitive to the composition and the annealing time.

In the literatures; it has been reported that a BSCCO superconductor has two superconducting phases of both high T_c(2223) and lower T_c(2212)[5-7]. Major understanding up to the present time that the high T_c phase is corresponding to the triple Cu-O layers sandwiched by Bi_2O_2 layers, and the lower T_c phase is corresponding to the double Cu-O layers[17,21]. In additional to the above two superconducting phases, Nobumasa et al.[13] reported that a semiconducting phase (2201) is corresponding to a structure having single Cu-O layers. Also they attributed the presence of 4.8° peak in X-ray diffraction related to the triple Cu-O layers in the high T_c phase.

The XRD analysis for all the prepared samples in this study shows the presence of the two superconducting phases; 2212 ,2223 also shows the presence of the semiconducting phase; 2201. All the samples show a diffraction peak at 5.9° which is related to the double Cu-O layers, 2212 phase, and this explains the superconducting behavior of the samples. Sample EM5 shows a diffraction peak at 4.8° which is related to the high T_c (2223) phase, as reported by Nobumasa et al.[13]. The presence of Ba in the composition of sample EM5 may be responsible for the formation of this phase.

The composition, annealing time and T_c's are summarized in Table (V-A-2). The effect of both annealing and doping Pb on superconducting behavior has been investigated using samples EM1, EM2, EM3 and EM4. First by increasing the concentration of Pb^{+2} from 0.0 to 0.3 mole ratio the value of T_c increases; this agrees with that reported by Kovacheva et al.[124]. However, on further increasing in the concentration of Pb^{+2} from 0.3 to 0.5 atomic ratio a decrease in the T_c value has been observed. Moreover by increasing the annealing time on sample EM2 which containing 0.3 mole of Pb^{+2} the T_c shifts to higher value. The introducing of Pb^{+2} in the samples which has different charges and ionic radius than Bi^{3+}, leads us to assume that

Pb^{2+} affects not only the geometry of the BiO layers but also induces charged defects due to violation of the electroneutrality requirements. Both effects probably results in the depression of superconductivity. This results is in agreement with that reported by Kovacheva et al.[124]

Also Yamada et al.[34] reported that additional Pb induces an insulator phase transition from a superconductor. This could be attributed to the formation of mixed valence state in Bi besides the Cu mixed valence state, and thus may result in T_c enhancement.

By substituting Ba^{+2} instead of Pb^{+2} (compare samples EM3 and EM5) the T_c was shifted to higher temperature. It means that Ba^{+2} enhancement the T_c value. This may be explained in the light of the ionic radius where Ba^{2+} is large in size more than Pb^{2+}. The presence of Ba in the sample improves the concentration and types of superconducting phases in a way improve the concentration and the type of superconducting phases. The XRD of sample EM5 shows a presence of high T_c phase 2223 (at 4.8°) which is not observed in all other samples.

The great variation in the concentration of Cu and Ca in the two samples EM3 and EM6 did not cause a large change in the T_c value. It means that the Cu and Ca has less effect in improvement the

superconducting properties such as the introducing of Pb^{2+} and Ba^{2+} as mentioned above.

Generally, it can be said that the superconducting properties depend on both annealing condition and the change in the composition (Table (V-A-2). These results indicate the important rule of annealing time in the preparation of the superconductor.

PART (B)

V-B-1- Cuprate Surface Reactivity to Protons:

Prior RRDE methods applied to cuprate behavior monitored solution reactivity through solubilized copper species detection and comparison to the separately determined limiting current density of proton reduction at a gold disk.[106] This allows determination of reaction stoichiometry, but requires an accurate value of the geometric collection efficiency, N , of the RRDE.[121] Ring voltammetry has been extended to proton reduction as well in the present work so that a combination of shielding and collection data at the ring allows full internal calibration without the accurate N determination for the RRDE, which can be difficult with these ceramic samples and method of fabrication. However, both new and old approaches were applied for confirmation of results.

The number of protons, n_D, involved in the dissolution reaction is expressed by:

$$La_2CuO_4 + n_D H^+ \rightarrow 2La^{+3} + Cu^{+2} + 1/2\ n_D\ H_2O + (8-n_D)\ e^- \qquad [15]$$

n_D could be less if species such as $La(OH)_n(H_2O)_m^{3-n}$ were solubilized in the reaction. The value for n_D can be derived from ring current-potential curves for the fixed proton concentration and blank cases (no added acid) in combination with the cuprate electrode (a) exposed to the aqueous electrolyte or (b) protected from it by the acrylate coating.

Defining shielded ring current, $i_{R(sh)}$, as that when the disk electrode is exposed to the H^+/ 1M NaCl solution and the unshielded ring current, $i_{R(unsh)}$, as that when the disk is isolated by the acrylic coating, we can relate them from ring-disk theory [119-121] as follows:

$$i_{(sh)} = (\beta^{2/3}-N)i_{D,H}^{+} \qquad [16]$$

and

$$i_{R(unsh)} = \beta^{2/3} i_{D,H}. \qquad [17]$$

The geometric factor, $\beta^{2/3} = [r_3^3/r_1^3 - r_2^3/r_1^3]^{2/3}$, where r_1 is the disk radius and r_2 and r_3 are the inner and outer radii of the ring electrode, respectively. Eqns [16] and [17] give the proton reduction contribution at the ring as a function of the limiting current for proton removal at the disk, $i_{D,H}^{+}$.

$\Delta i_R = i_{R(unsh)} - i_{R(sh)}$ is the difference in the limiting current for proton reduction at E_R= -1.00V vs Ag/AgCl at the ring in two experimental cases. Thus, from [16] and [17],

$$\Delta i_R = N i_{D,II}^{+} \quad . \qquad [18]$$

Cu^{+2} is produced by reaction [15] stoichiometry and detected at the ring by the two-step reduction to copper metal,

$$Cu^{+2} + 2e \rightarrow Cu(0) \quad , \qquad [19]$$

as measured at -0.7 V vs Ag/AgCl in Figure (V.B-1) type experiments. We use the $n_R = 2$ ring reduction of solubilized Cu(II) at this potential since it is much better defined than the first 1- electron step in the chloride medium. It has been previously shown that, with the "effective collection efficiency," N_E, defined as

$$N_E = n_R/n_D \quad N, \qquad [20]$$

$$N_E = [i_{RCu(II)}/i_{D,II}^{+}]. \qquad [21]$$

Then

$$N = [(i_{RCu(II)}/i_{D,H+})(n_D/n_R)] \qquad [22]$$

and substituting from [18], the final simplification will be

$$n_D = n_R [\Delta i_R/(i_{RCu(II)})] \, . \qquad [23]$$

Thus, we see that n_D is determined without direct knowledge of the geometric factors N and $\beta^{2/3}$, or a separate measurement of $i_{D,H+}$, on

another electrode whose disk area would need be compared to that in the RRDE. Only ring data are needed in the method, culminating in [18], which simplifies the experiment considerably and should lead to higher accuracy.

Figure (V-B-1) shows the limiting currents of H_2 evolution and Cu(II) reduction when the disk is first isolated, then when it is exposed to the solution in order to obtain the difference current, Δi_R, and $i_{RCu(II)}$. Curve (c) represents the blank where there are no protons, and in this case there is no soluble copper. Also curve (c) is independent of the rotation speed. When the disk is exposed with the addition of protons, curve (b) shows disk-solubilized Cu(II) reduced to Cu(0). Curve (a) shows the higher limiting current of the protons when the disk is protected.

Figure (V-B-2) summarizes the results for proton reduction at E_R = -1.1 V vs Ag/AgCl ($i_{R,unsh}$) as a function of $[H^+]$ and the square root of electrode rotation speed ($\omega^{1/2}$) with the disk covered at open circuit. Figure (V-B-3) then shows $i_{R(sh)}$ of protons similarly as a function of $[H^+]$ and square root of electrode rotation speed ($\omega^{1/2}$) with the La_2CuO_4 disk exposed at open circuit. For the same variations, Figure (V.B-4) shows $i_{RCu(II)}$ from the ring current monitored at -0.56 V vs

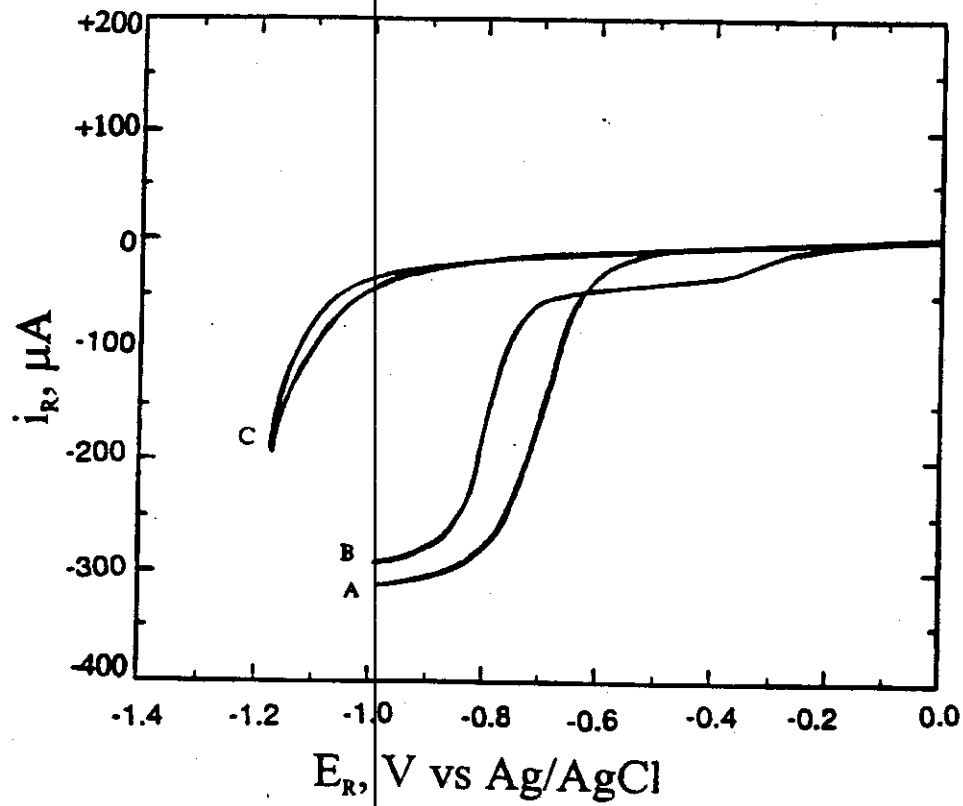

Figure (V-B-1): Ring potential scans at 10 mV/s for a La_2CuO_4 disk-Au ring electrode rotated at 900 rpm in 0.1mM H^+/1.0 M NaCl. (A)La_2CuO_4 disk lacquer coated, (B) La_2CuO_4 disk exposed, (C) La_2CuO_4 disk -Au ring electrode in 1.0M NaCl.

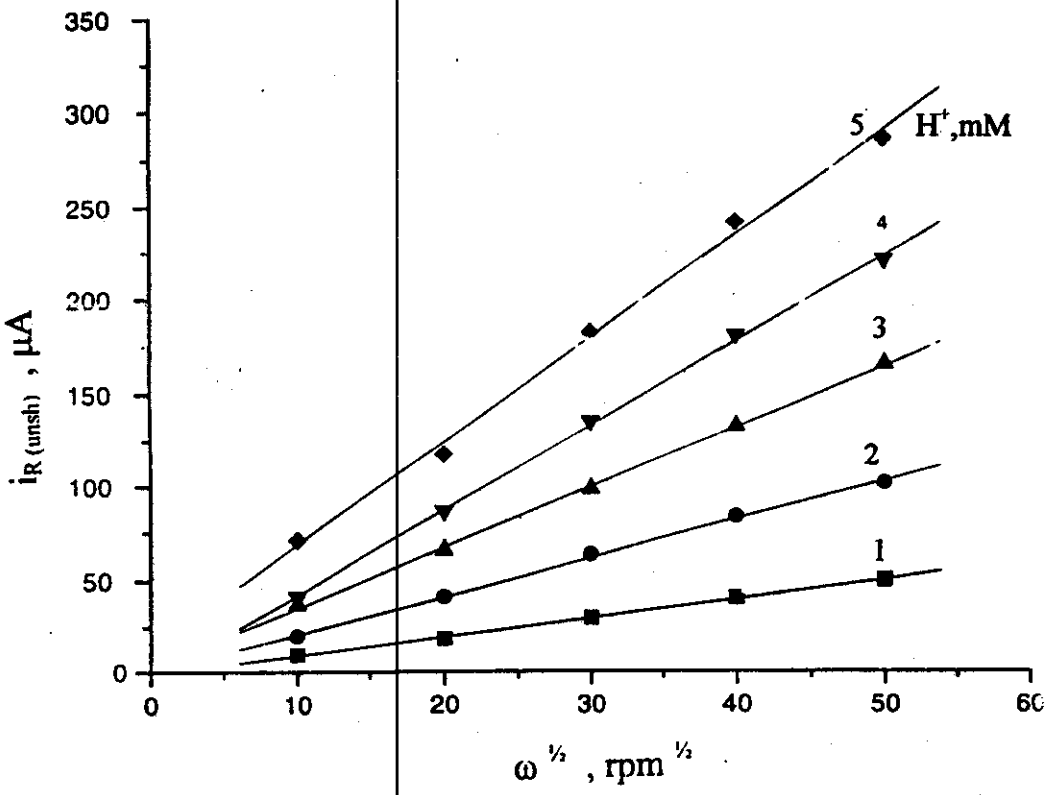

Figure (V-B-2): $i_{R(unsh)}$ - $\omega^{1/2}$ plot for La_2CuO_4 at different $[H^+]$, marked as **mM, in 1M NaCl; disk is held at open circuit and i_R** measured at –0.56 V vs Ag/AgCl.

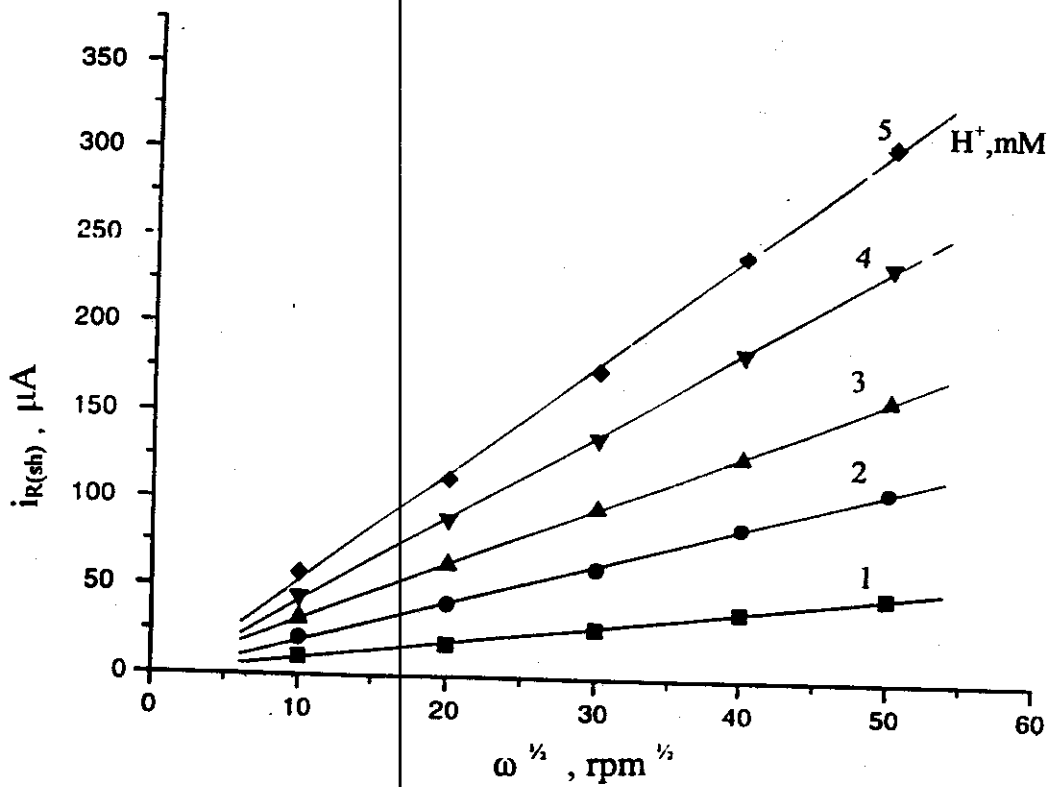

Figure (V-B-3): $i_{R(sh)}$ - $\omega^{1/2}$ plot for La_2CuO_4 at different [H^+], marked as mM, in 1M NaCl.

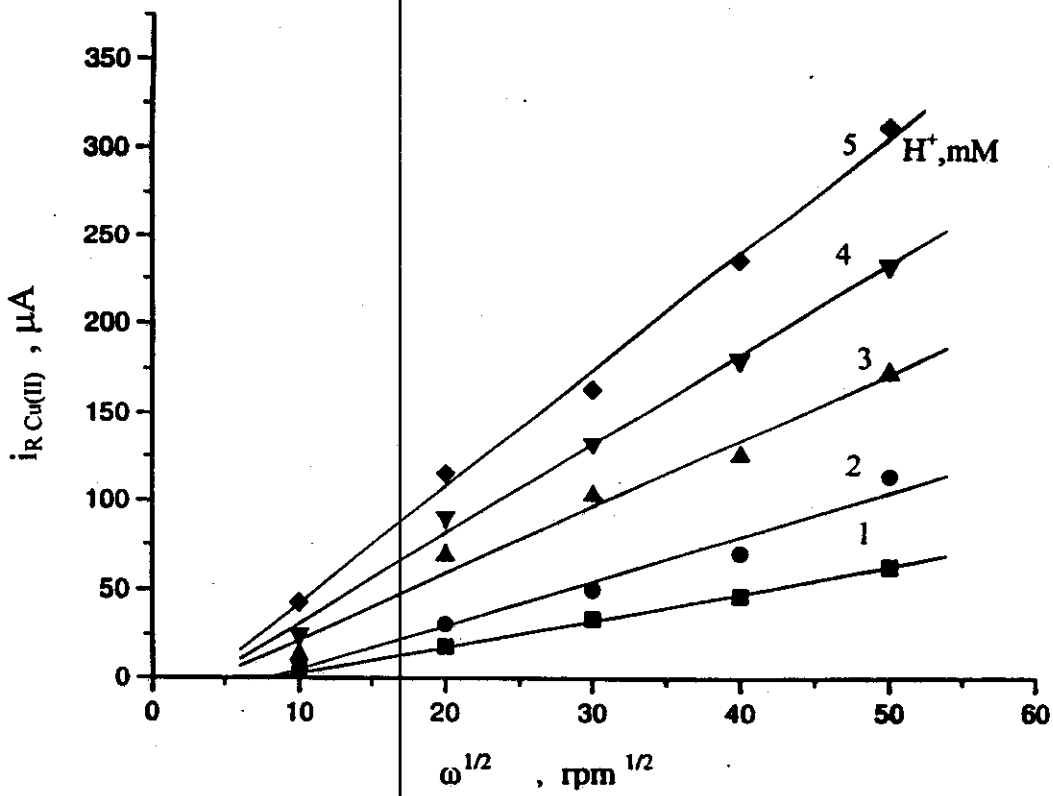

Figure (V-B-4): $i_{RCu(II)}$- $\omega^{1/2}$ plot for La_2CuO_4 at different [H^+], marked as mM, in 1M NaCl, disk is held at open circuit and i_R measured at -1.1V vs Ag/AgCl.

Ag/AgCl. Notably, all three plots Figures(V-B-(2-4)) are linear and indicative of a proton mass transfer controlled reaction at the disk.

With Δi_R taken from the difference of the corresponding slopes in Figures (V-B-2) and (V-B-3), Figure (V-B-5) then shows an liner relation between Δi_R and $i_{RCu(II)}$. From the slope of this plot, 3.9, and the given n_R=2, n_D is inferred to be 7.8, consistent with [24]:

$$La_2CuO_4 + 8\,H^+ \rightarrow 2\,La^{+3} + Cu^{+2} + 4\,H_2O\,. \qquad [24]$$

This reaction sequence for the stoichiometry of the dissolution process of the unoxidized pellet is fast enough to be limited by H^+ transport. Such reactivity is thus comparable to that of $Ba_2YCu_3O_7$ and other oxidazed cuprates[107] similarly observed, and much higher than that of CuO which dissolves in acid at a distinctly kinetically controlled rate.[125]

With application of the earlier-used approach requiring a separate noble metal disk for hydrogen ion reduction (i_{D,H^+}), Figure (V-B-6a) shows the results obtained for $i_{RCu(II)}$, as a function of $[H^+]$ and $\omega^{1/2}$ with the La_2CuO_4 disk at open circuit (i_D= 0). Figure (V-B-6b) shows a plot of $i_{Rcu(II)}/\omega^{1/2}$ vs $[H^+]$ from this data. The geometric collection efficiency, N ,of the La_2CuO_4 disk - gold RRDE is 0.34 and the measured slope for the separately measured reduction of H^+ at a gold

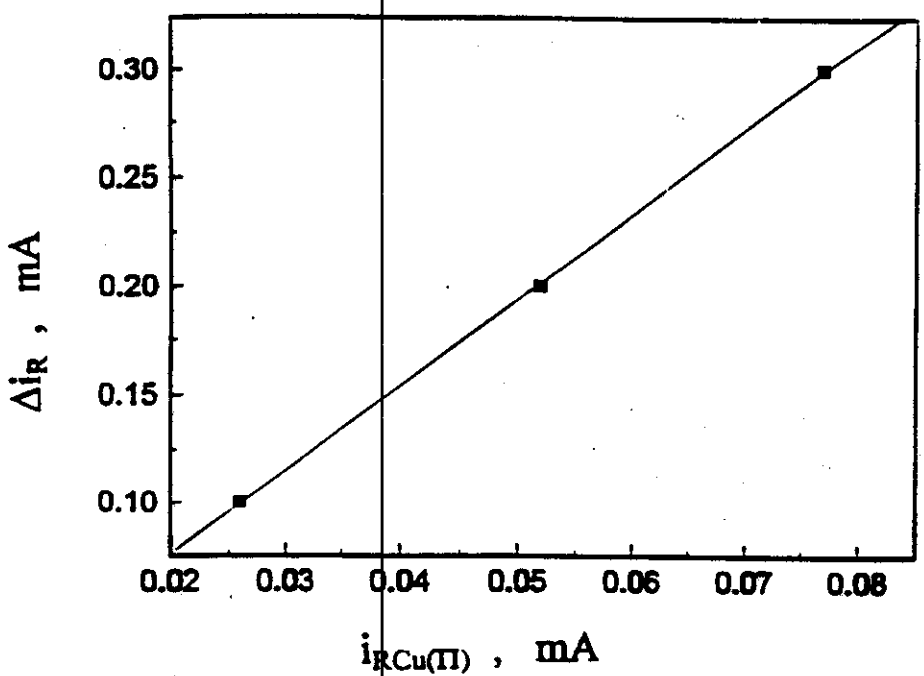

Figure (V-B-5): $\Delta i_R - i_{RCu(II)}$ plot for La_2CuO_4 at 1,2,3 mM $[H^+]$, in 1M NaCl.

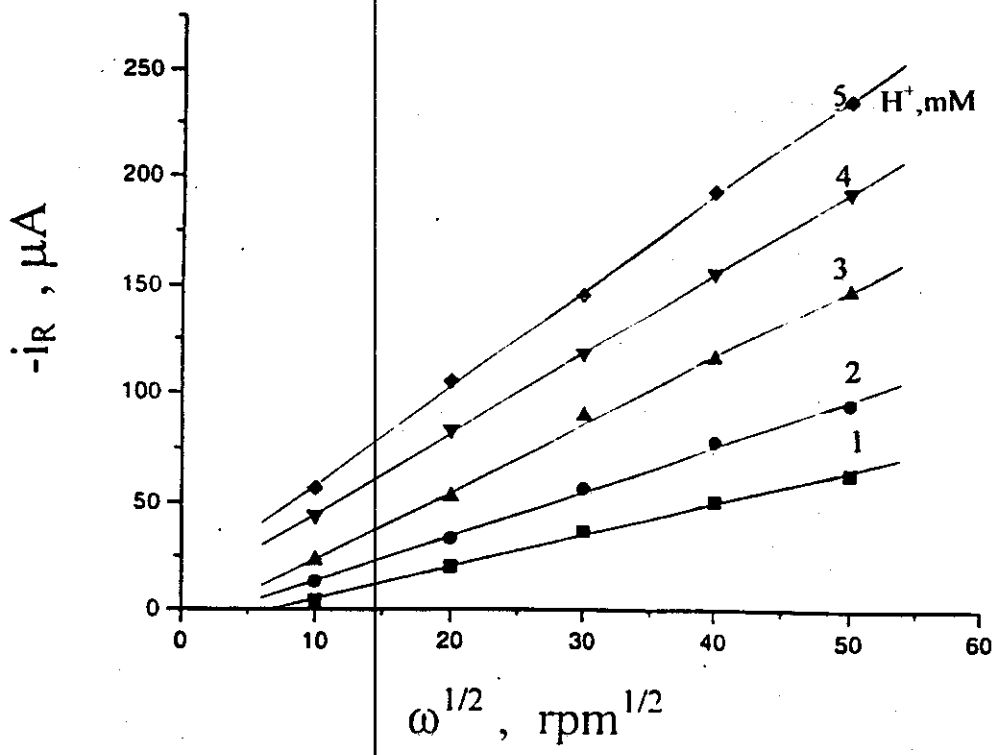

Figure (V-B-6a): i_R- $\omega^{1/2}$ plot for La_2CuO_4 at different [H^+], marked as mM, in 1M NaCl, i_R measured at – 0.52 V vs Ag/AgCl.

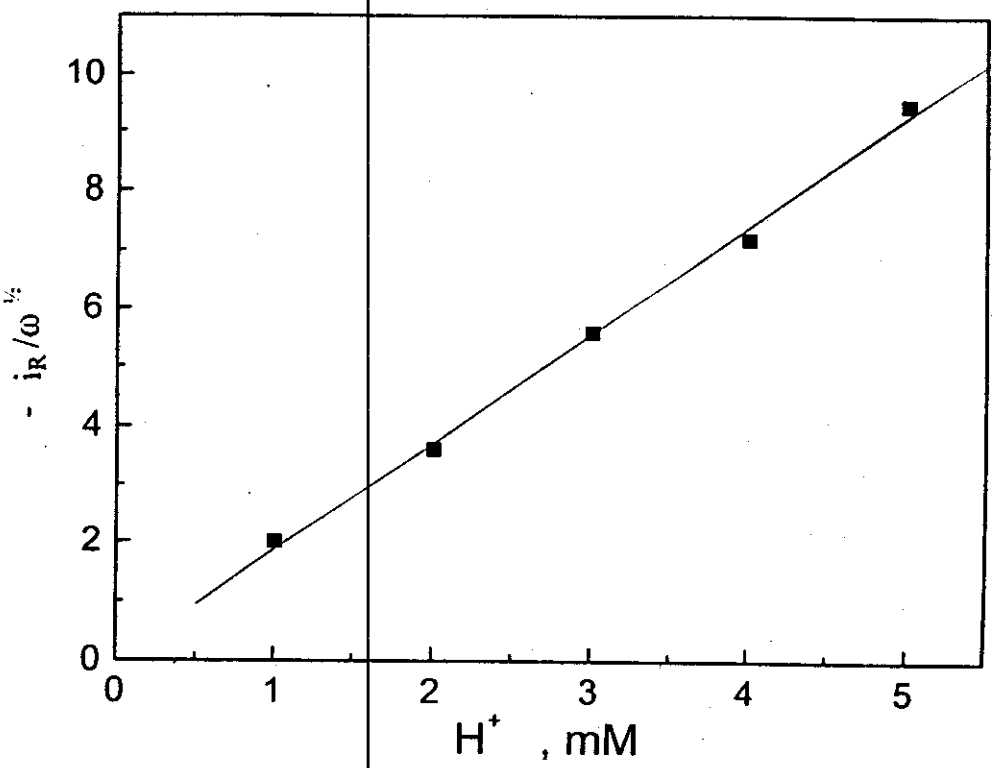

Figure (V-B-6b): $i_R/\omega^{1/2}$ - $[H^+]$ plot for La_2CuO_4.

disk in 1 M NaCl is 9.11 μ A /rpm$^{1/2}$ mM. The gold and La_2CuO_4 disks were fabricated to match in geometric area the precision stainless shafts to which they are attached. The value of $i_R/\omega^{1/2}C$ from Figure (V-B-6b) is 0.752 μA / rpm$^{1/2}$ mM , giving an experimental ratio, N_E , of 0.0825. Thus n_D = 8.2, a result consistent with the value 7.8 obtained above from the measurements with a single RRDE. This agreement of both approaches gives a similar conclusion for reaction stoichiometry. This suggests that the new route through the single electrode is considerably simpler experimentally, with its independence of precisely known geometries and concentricities, and at least equivalent in accuracy.

V-B-2- Coulometric Efficiency and Rate of La_2CuO_{4+x} Formation:

The coulometric efficiency of formation of the La_2CuO_{4+x} superconductor can be indirectly approached by monitoring oxygen reduction at the ring. The electrochemical process described by Grenier et al. [82] is

$$La_2CuO_4 + 2x\ OH^- \rightarrow La_2CuO_{4+X} + xH_2O + 2xe^- \qquad [25]$$

The competitive reaction at the anode is

$$4OH^- \rightarrow H_2O + O_2 \uparrow + 4e^- \ . \qquad [26]$$

Figure (V-B-7) shows the anodic current density of La_2CuO_4 in 1M KOH vs potential to characterize the film formation process of the superconductor. The only product of [25] and [26] detectable at the gold ring is oxygen which gives well-defined 2e and 4e reduction steps. Determining the disk component of current resulting from [26] from ring data then allows the superconductor formation current in [25] to be determined by difference.

Figure (V-B-8) shows the 4e limiting current for oxygen reduction at the ring plotted in the form i_R- i_D during successive disk potential scans, such as that displayed in Figure(V-B-7). The scans reach progressively more positive potentials at the disk. These all show there is no ring response to the anodic disk current until a certain number of coulombs have accumulated. At that point the ring current rises rapidly to the theoretical collection value for oxygen reduction. Repeating this scan successively moves this point essentially to the initiation of anodic current at the disk, thus progressively shrinking the cyclic loop in i_R where oxygen is not detected.

The difference between the oxygen reduction current and the limiting amount for 100% oxygen efficiency can be attributed to

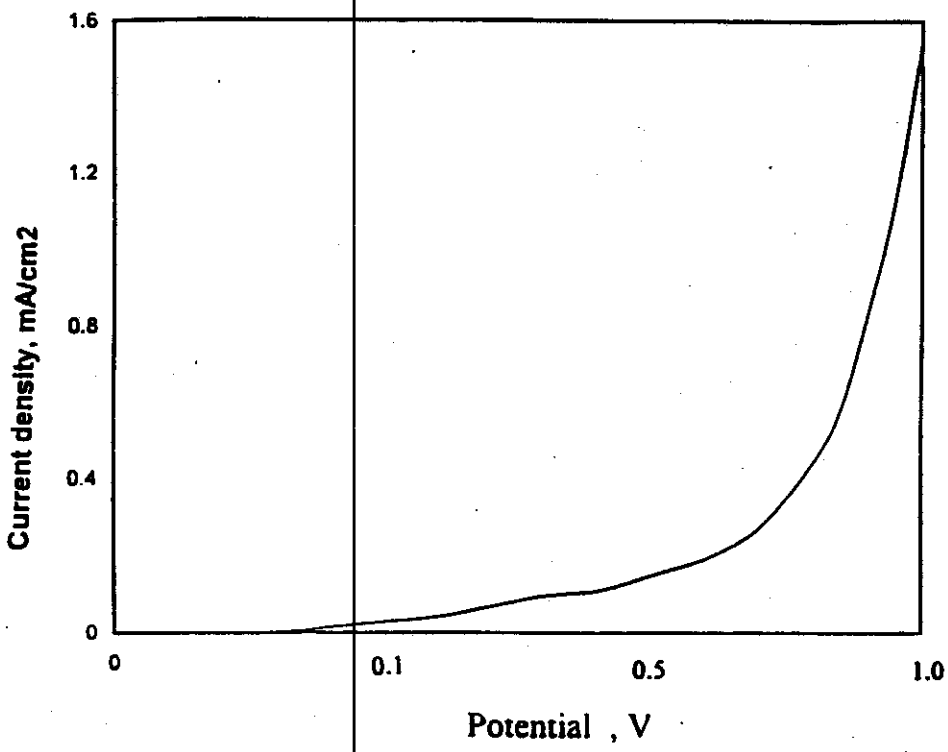

Figure (V-B-7): Potentiodynamic curve characterizing film formation of the superconductor in 1 M KOH, scan rate 5 mV/sec. Electrode area = 0.178 cm^2.

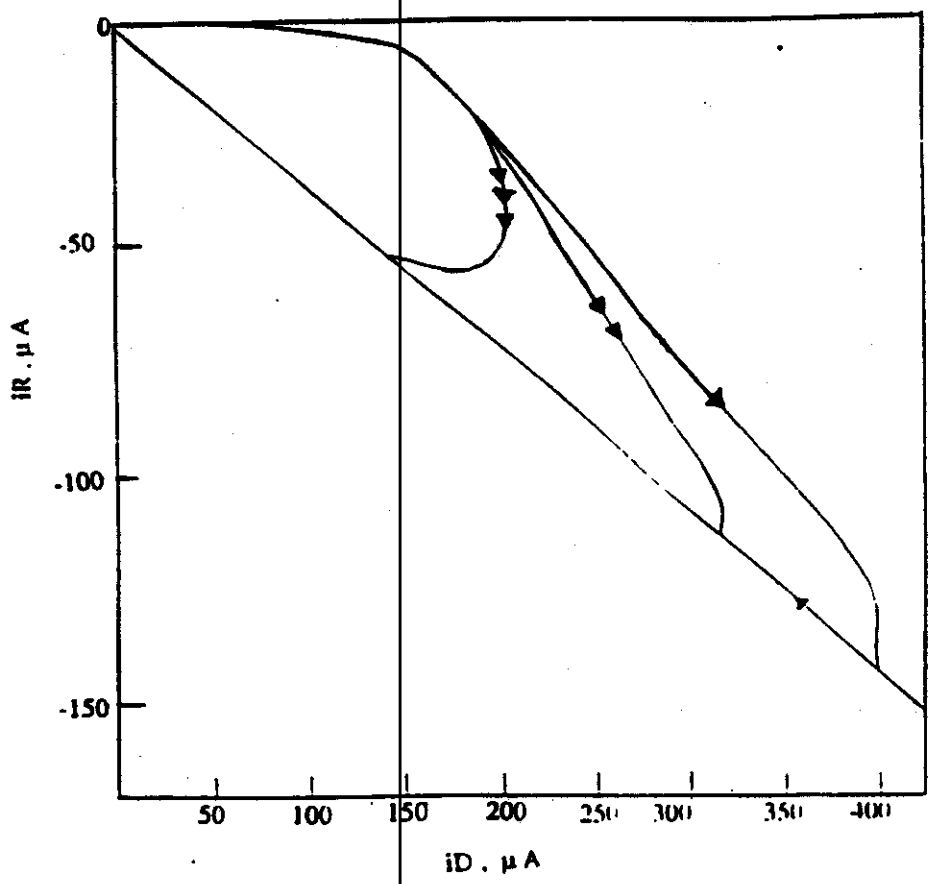

Figure (V-B-8): Three successive i_R- i_D curves for a La_2CuO_4 disk-Au ring in 1M KOH. E_R, -1.2 V; ω, 900 rpm. Potential-controlled disk was scanned at 5 mV/sec. Arrows on curve indicate scan direction.

superconductor formation. The disk coulombs assumed to go into the surface oxidation process are then given by [126]

$$\int i_D\,dt - \int i_R/N\,dt \qquad [27]$$

where $\int i_D\,dt$ represents the total faradaic charge passing at the disk during the positive potential scan and $\int i_R/N\,dt$ represents the ring-determined disk charge attributable to oxygen evolution via [26]. The difference is charge going into formation of La_2CuO_{4+x} at 2x Faradays/mole superconductor. These experiments are easier to quantitate during constant anodic current at the disk, where disk coulombs are simply $i_D \cdot \Delta t$, where Δt is the time of anodization. Such galvanostatic oxidation data similarly shows initial incomplete oxygen collection (a capacitive charging component of disk current must be accounted for), which can be attributed to superconductor formation. This kind of experiment is shown in Figure (V-B-9), in which E_D and i_R are plotted vs time, t, and t = 0 represents the switch from open circuit to constant anodic current. From the missing oxygen reduction current of i_R shown in Figure (V-B-9) it can be estimated that, on average, 6.6×10^{-3} coulombs/cm^2 go into formation of the

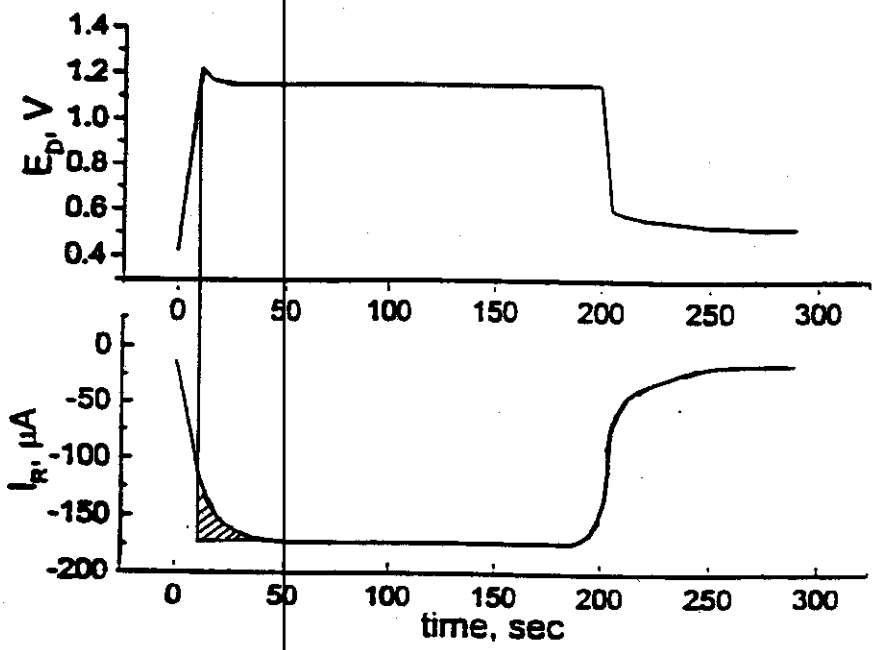

Figure (V-B-9): Galvanostatic data for La_2CuO_4 at 200 μA, E_D , i_R – t plots were obtained in 1M KOH. The area under the curve is the missing O_2 reduction current (superconductor formation).

superconductor phase, with only a small dependence on current density seen from Table (V-B-1), the calculated charge at different applied constant currents.

If a composition $La_2CuO_{4.12}$ is assumed,[80,92] and roughness of the ceramic disk is ignored, the converted layer is then a maximum of 163 nm thick. A large roughness factor is expected from the hot pressing technique of formation and actual thicknesses should be much lower. So the actual thicknesses will be a maximum of 163 nm thick divided by unkown roughness factor. Further growth of the layer appears slow from ring data at different disk currents and not consistent with an unexpectedly enhanced transport of anionic species through the solid phases.[91] This conclusion needs to be confirmed with independent measurements of the presence of La_2CuO_{4+x}, which are continuing.

Figure (V-B-10) shows the XPS spectra for a La_2CuO_4 pellet before and after oxidation. The pellet was oxidized by placing it in 1 M KOH solution, and passing a constant anodic current of 200 μA through it for 15 days. At this stage, in agreement with other references,[127,128] the measurements were not able to discriminate definitively between the states of oxidation in La_2CuO_4 and La_2CuO_{4+x}.

Table (V-B-1): Different constant current applied and total charges are derived for formation of superconductor phase.

Applied Current, μA	Calculated Charge, coulombs/cm^2 × 10^{-3}
50	5.63
100	5.85
150	6.30
200	6.60
500	6.61

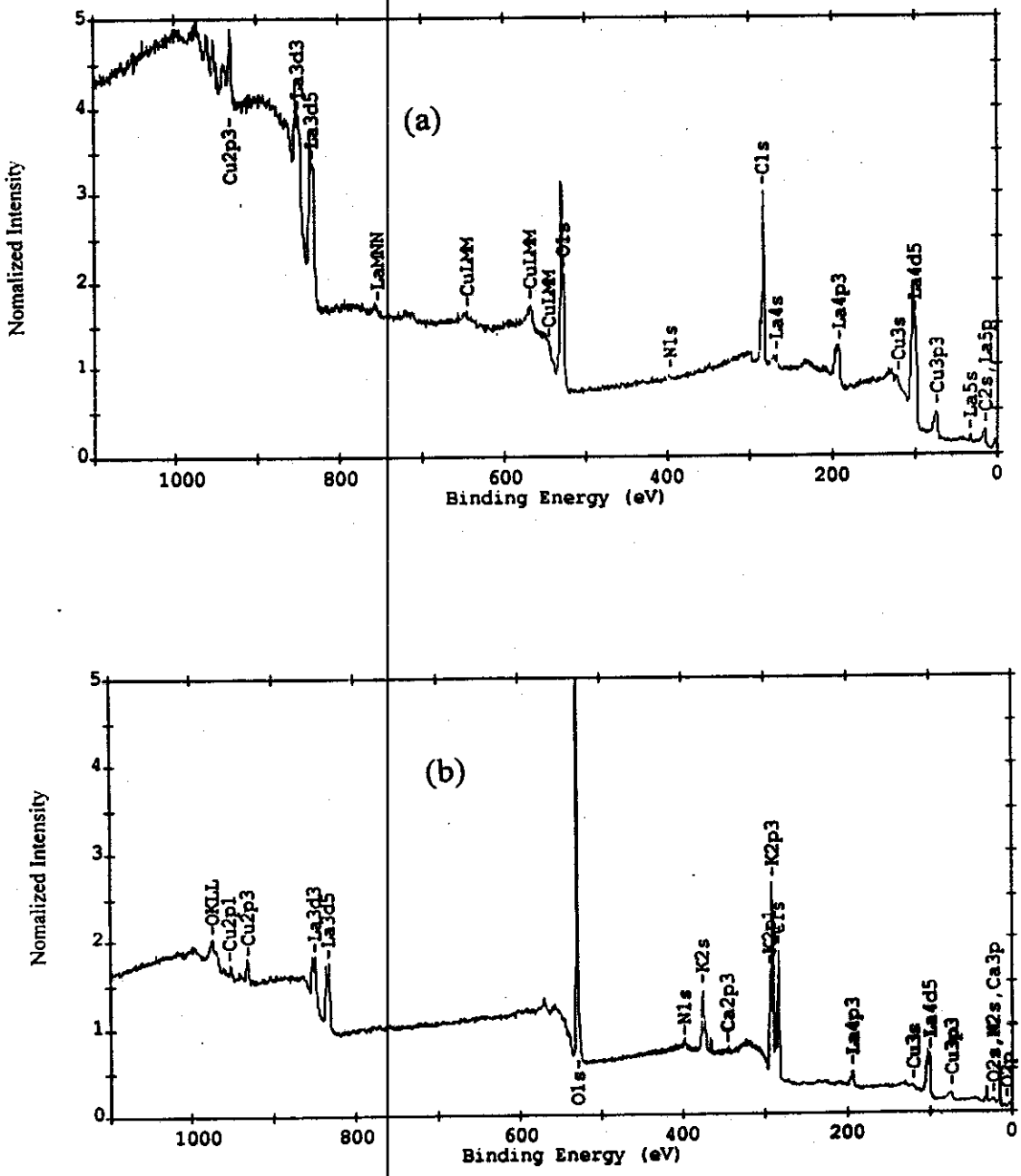

Figure (V-B-10): XPS spectra of La_2CuO_4 pellet (a) before oxidation and (b) after oxidation in 1 M KOH solution.

V-B-3- General discussion

Electrochemical oxidation is a powerful method for preparing oxides of higher oxidation states of transition metals, and we have shown methodology for following the extent of such reaction. La_2CuO_4 can be anodized at room temperature in an aqueous base using an electrochemical technique to form a superconductor phase and we can monitor the depth of this solid state conversion by measuring the competition to the oxygen evolution reaction. The rate of formation of superconductor phase La_2CuO_{4+x} is limited by slow solid-state diffusion. The maximum thickness of the superconductor formed here on ceramic disks was about 163nm thick from short time experiments. These measurements are consistent with the long periods of growth found necessary to convert macro amounts of precursor phase to superconductor.[129]

The La_2CuO_4 precursor of the superconductor is dissolved by aqueous acid at proton mass transport limited rates. An improved RRDE technique for such measurement has been demonstrated. This method employs a simplification which eliminates the previous requirement of a separate measurement of the limiting current of hydrogen ion reduction with a noble metal disk electrode, in

conjunction with necessary accurate geometric measurements and concentricity of the RRDE structure. The latter needs are not always simple to satisfy for the ceramic materials used here and cancellation of the N (collection efficiency) measurement by using ring behavior for all aspects is a significant improvement for accuracy and convenience of stoichiometry determination in the general case of cuprate surface chemistry evaluated by such techniques. La_2CuO_4 was shown to have many chemical and electrochemical properties in common with those the $Ba_2YCu_3O_7$ compound and is much more reactive than CuO toward protons.